MICROSTRUCTURE AND MECHANICAL PROPERTIES OF NI-BASED ALLOYS FABRICATED BY LASER POWDER BED FUSION

Sebastien Dryepondt, Holden Hyer, Fred List III, Stephen Taller, Amir Ziabari, Yi-Feng Su, Zackary Snow
Oak Ridge National Laboratory, Oak Ridge, Tennessee, USA

ABSTRACT

The Advanced Materials and Manufacturing Technologies (AMMT) program is aiming at the accelerated incorporation of new materials and manufacturing technologies into nuclear-related systems. Complex Ni-based components fabricated by laser powder bed fusion (LPBF) could enable operating temperatures at T > 700°C in aggressive environments such as molten salts or liquid metals. However, available mechanical properties data relevant to material qualification remains limited, in particular for Ni-based alloys routinely fabricated by LPBF such as IN718 (Ni-19Cr-18Fe-5Nb-3Mo) and Haynes 282 (Ni-20Cr-10Co-8.5Mo-2.1Ti-1.5Al). Creep testing was conducted on LPBF 718 at 600°C and 650°C and on LPBF 282 at 750°C, finding that the creep strength of the two alloys was close to that of wrought counterparts, with lower ductility at rupture. Heat treatments were tailored to the LPBF-specific microstructure to achieve grain recrystallization and form strengthening γ' precipitates for LPBF 282 and γ' and γ" precipitates for LPBF 718. In-situ data generated during printing and ex-situ computed tomography scans were used to correlate the creep properties of LPBF 282 to the material flaw distribution. In-situ data revealed that spatter particles are the potential causes for flaws formation in LPBF 282, with significant variation between rods based on their location on the build plate. XCT scans revealed the formation of a larger number of creep flaws after testing in the specimens with a higher initial flaw density, which led to a lower ductility for the specimen.

INTRODUCTION

The U.S. Department of Energy, Office of Nuclear Energy's AMMT program aims at accelerated qualification of new materials and manufacturing technologies into complex products and systems [1]. Additive manufacturing (AM) is among the advanced manufacturing techniques of interest, enabling the fabrication of complex, near-net-shape components and thus reducing the need for processing steps such as machining, welding, and brazing [2]. While the use of Ni-based alloys is currently limited to a few alloys in current nuclear reactors [3,4], the harsh environments expected in Gen IV reactors necessitate high temperature Ni-based components [5]. The AMMT program has been evaluating the potential of various Ni-based alloys to be produced by additive manufacturing and in particular laser powder bed fusion (LPBF) [6]. Three categories were identified, low Co bearing Ni-based alloys for potential use close to the reactor core, high temperature high strength Ni-based alloys allowing operating temperature >~700°C, and low Cr bearing alloys with superior compatibility with molten salt. Several Ni-based alloys were processed via LPBF and characterized with this paper presenting a summary of the results for LPBF 718 and LPBF 282.

Alloy 718 is the most used Ni-based alloy in the aerospace industry, with superior strength due to the presence of γ' and γ" precipitates. Moreover, LPBF 718 has been extensively studied [7-14]. Literature reviews on LPBF 718 can be found elsewhere [6,14]. Due to the unique, often heterogenous, microstructure found in LPBF 718, numerous studies have been focused on heat treatment to achieve recrystallization and homogenize the microstructure [8-12]. Tensile testing has been extensively conducted on LPBF 718 as discussed by Hosseini and Popovich in their

review paper [14], but publicly available fatigue and creep data are rather limited [14-20]. The LPBF 718 data often showed lower creep strength and ductility compared to wrought 718, both in the as-build and annealed conditions. Creep testing was therefore conducted on as-printed and annealed LPBF 718 on material that exhibited great tensile properties [11].
The γ' strengthened 282 alloy was also fabricated by LPBF for creep testing evaluation. Due to a relatively low γ' volume fraction, ~20% [21], the alloy is quite printable [22] and has been considered for various high temperature applications requiring complex geometries, such as heat exchangers [23,24]. As for the LPBF 718, available data on the long-term properties of LPBF282 are very limited [25,26]. Non-destructive X-ray computed tomography (XCT) was carried out before and after creep testing to establish correlation between the specimen flaws and the LPBF 282 creep behavior, while in situ data generated during printing was analyzed to understand possible causes of flaw formation.

EXPERIMENTAL METHODS

Materials & specimens

Figure 1 shows the LPBF 718 and 282 materials used for creep specimens machining. A large block of alloy 718 was fabricated by LPBF using a Concept X-Line 2000R at the Oak Ridge Manufacturing Demonstration Facility (MDF). Printing parameters and powder chemistry are summarized below:
A laser power of 370 W, spot size of 0.3 mm, scanning speed of 500 mm/s, hatch spacing of 0.16 mm, scan rotation between layers rotation of 67◦, powder chemistry: Ni-18.22Fe-18.99Cr-5.15Nb-3Mo-0.93Ti-0.5Al-0.1Co-0.04Si-0.04C-0.012N-0.016O.
The printed piece was sectioned into four identical pieces, each 59mm×18mm×15mm in size. One sample was exposed to the following heat treatment: homogenization at 1174 °C for 2h and 1204 °C for 6h, solution anneal at 1093 °C for 1h and aging at 718 °C and 621 °C, both for 8h. Additional information on the selection of the heat treatment can be found elsewhere [11], and the grain structures before and after annealing are shown in Figure 2a and 2b, respectively. While elongated grains along the build direction were observed in the as-printed condition, with an average equivalent grain diameter of 8.3 ±.22μm, annealing resulted in an equiaxed grain structure with an average grain size of 37.9. ± 2.6 μm [11].
Small scale SS3-type dog bone specimens with a gage section of 1mm×2mm and a gage length of 7.62mm were machined with a 600grit finish from as-printed and annealed ~9mm×29mm×15mm blocks (Figure 1a and 1b). Small creep specimens such as the one shown in Figure 1c were machined along the build direction for the annealed specimens and both along and perpendicular to the build direction for those machined in the as-printed condition. The annealed material was not tested perpendicular to the build direction as the recrystallized microstructure is expected to result in isotropic mechanical properties.
As can be seen in Figure 1d plates and rods of Haynes 282 were fabricated using an LPBF Renishaw AM250 machine (pulsed laser) with the following optimized printing parameters and powder chemistry provided by the manufacturer: laser power of 200W, layer thickness of 60μm, hatch spacing of 86μm, point spacing of 70μm, exposure time of 80μs and powder chemistry: Ni-19.37Cr-10.24Co-8.33Mo-2.11Ti-1.54Al-0.05C -0.03Si-0.01O in wt%. The Renishaw AM250 was equipped with three imaging modalities connected to an edge computing system at the machine. These sensors include a 20 megapixel visible light camera, a 4.2 megapixel near-infrared (NIR)-sensitive camera, and a long-wave infrared camera.

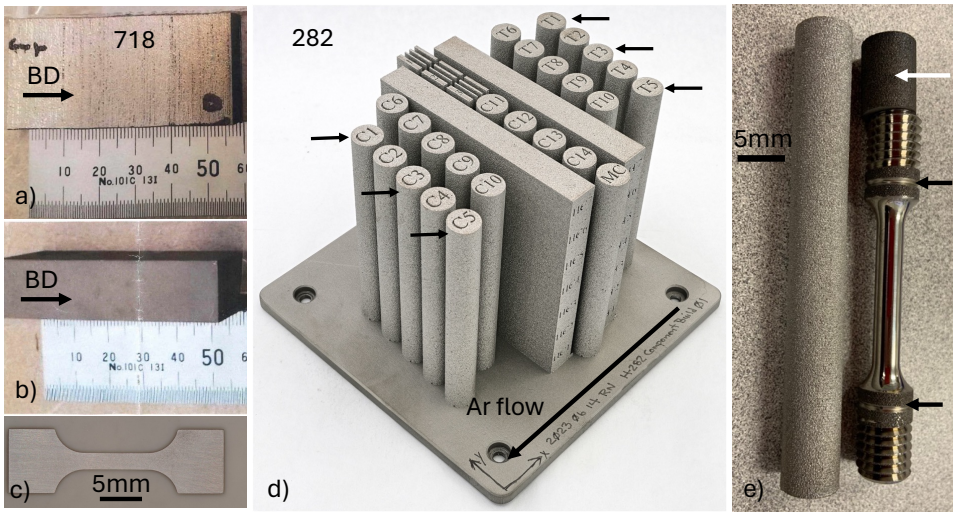

Figure 1: a) and b) LPBF 718 blocks used for specimens machining, a) as printed, b) annealed, c) small scale creep specimen, d) LPBF 282 build and e) standard creep specimen machined from one of the rods. Black arrows in a) show rods from which creep specimens have been machined. Black arrows in b) highlight groves for deformation measurement. White arrow in b) shows leftover after specimen machining used for microstructure characterization

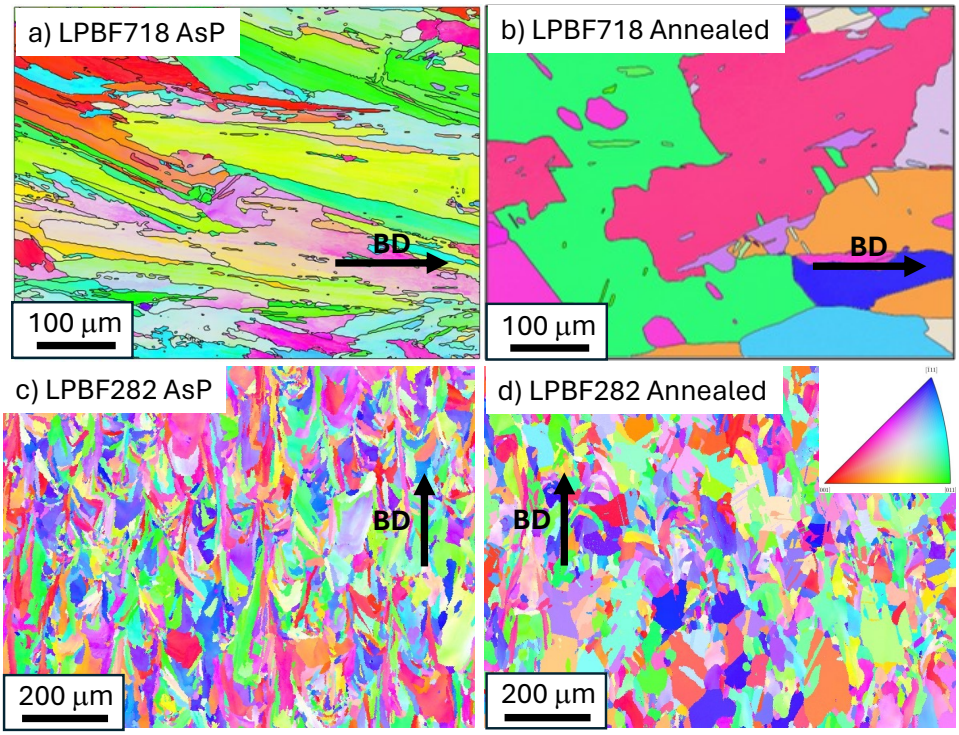

Figure 2: Electron Backscatter Diffraction (EBSD) maps, a) LPBF 718, as-printed (AsP), b) LPBF 718, annealed, c) LPBF 282, as-printed, d) LPBF 282, annealed.

Rods C1, C3, C5, T1, T3 and T5, highlighted in Figure 1d were heat treated for 1h at 1180°C in Ar and cooled in air as recommended by the Idaho National Laboratory (INL) based on heat treatment experiments using LPBF 282 material provided by EOS GmbH. The heat treatment was designed to obtain nearly full recrystallization with limited grain growth [6]. As can be seen in Figure 2c and 1d, elongated grains were observed in the as-printed conditions with an average equivalent grain diameter of 11.6μm ± 11.2μm. Only a slight increase in average grain size was measured after annealing, 13.8μm ± 13.6μm for the T1 specimen, and 12.5 μm ± 12.2μm for the C1 specimen, indicating that most of the small grains did not recrystallize.
Full size standard creep specimens with a cylindrical gage section of 0.63mm in diameter and a gage length of 32mm (Figure 1e) were machined from the annealed rods and a final one step heat treatment of 4h at 800°C was performed in vacuum for γ' precipitate formation [27].

Microstructure characterization

X-ray Computed Tomography (XCT)

Industrial XCT is a nondestructive method that captures radiographic images of objects from various angles, and these images are then used to algorithmically reconstruct 3D representations of the scanned objects. For all XCT, a ZEISS Metrotom system with an X-ray source of 200kV, with a short-scan strategy with 145 views between (0 and 197degrees), each view was average of 8x1second acquisition, resulting in a scan time of 18minutes scans. Using advanced deep learning-based algorithms developed in [28], a reconstruction of the samples was performed for XCT scans before and after creep testing, with a detection limit of ~50μm.

Electron microscopy

A Tescan Mira model 3 scanning electron microscope (SEM), equipped with energy dispersive X-ray spectroscopy (EDS) and EDAX Velocity Plus EBSD camera and operated at 20 kV with APEX software was used to characterize the LPBF 718 before and after creep testing. The inverse pole figure (IPF) maps were processed using MTEX for the LPBF 718 and an EDAX OIM analysis software version 8 for the LPBF 282. The specimens for scanning transmission electron microscopy (STEM) analysis were prepared using a Hitachi focused ion beam (FIB) operated at 40 kV. The STEM-EDS analysis was carried out using an FEI Talos FX200 STEM operated at 200 kV. The microscope was equipped with an extreme field emission gun (X-FEG) electron source and a Super-XEDS (energy dispersive spectroscopy) system with four silicon drift detectors (SDD).

Creep testing

Creep testing was conducted in air using a dead load machine for small scale LPBF 718 specimens at 600°C or 650°C and stress varying from 600 MPa to 700 MPa. Two thermocouples attached to the top and bottom grips were used to control the temperature within ±3°C. Semi-quantitative creep curves were generated using two linear variable differential transformer (LVDT). These LVDT

followed the displacement of two rods clamped to the top and bottom specimen grips. Lever arm machines were used for creep testing of the full size LPBF 282 specimens and testing was conducted according to ASTM standard E139. Thermocouples were attached to the gage section and the rods connected to the LVDT were clamped to the specimen head using the grooves highlighted in Figure 1b. Testing was conducted at 750°C with applied stresses of 300MPa or 350MPa.

RESULTS

Creep testing of LPBF 718

Creep results are summarized in Table 1, and the LPBF 718 creep lifetimes are compared in Figure 3 with wrought 718 creep data [29] using a Larson Miller plot according to the equation:

$$LMP = T\,(°K) \cdot \left(C + \log t_r\,(h)\right) \quad (1)$$

Where C =20, T is the testing temperature, and t_r is the time to rupture.
The creep strength for the LPBF 718 in the annealed condition was similar to the wrought 718 creep strength, with the longest test, still ongoing, reaching 7,100h. Lifetimes for the as-printed specimens were only slightly lower than the lifetimes for the annealed specimens and limited impact of the specimen orientation with respect to the build direction was noticed for the as-printed LPBF 718. The main concern highlighted in Figure 3b is the limited ductility at rupture measured for the LPBF 718, consistent with data published in the literature on LPBF 718 [17-20]. Wrought 718 is expected to exhibit strain at rupture of ~20% [30], but the alloy ductility is dependent on the both the heat treatment and testing conditions [31,32].

Table 1*:* Summary of LPBF 718 creep results

Condition	Orientation	Temp. (°C)	Stress (MPa)	lifetime (h)	LMP
As Fabricated	BD	650	650	385	20850
As Fabricated	BD	600	750	724	19960
As Fabricated	Per. To BD	650	650	357	20819
As Fabricated	Per. To BD	600	750	524	19837
Annealed	BD	650	650	18	19622
Annealed	BD	650	650	463	20924
Annealed	BD	600	750	991	20079
Annealed	BD	650	600	536	20982
Annealed	BD	600	650	7625 ongoing	20853

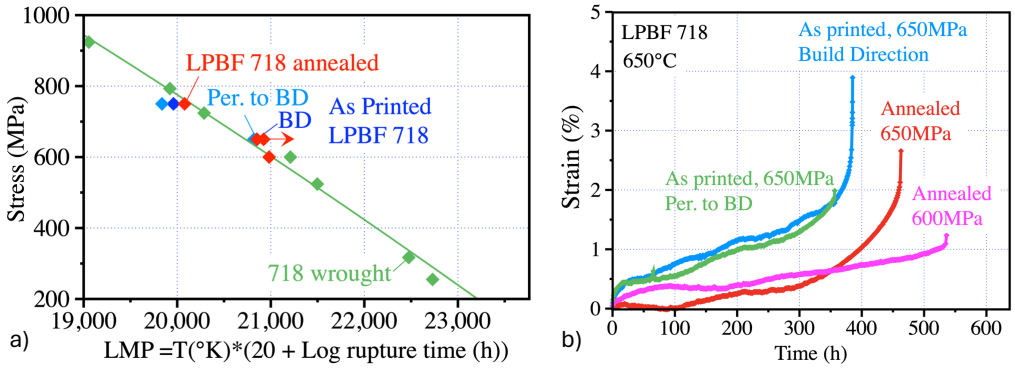

Figure 3: a) Larson Miller plot comparing the creep strength of LPBF 718 and wrought 718, b) example of creep curves for the annealed and as-printed LPBF 718 at 650°C. Per. to BD = perpendicular to build direction

SEM and STEM micrographs of the ruptured creep specimen tested in the annealed condition at 650°C, 650MPa for 463h is shown in Figure 4. The SEM micrographs highlight the presence of large precipitates and cracks at grain boundaries. The EDS compositional maps revealed that these precipitates were likely brittle (Nb,Ti)-rich carbides. In addition, STEM micrographs and the corresponding EDS maps highlighted the presence of a high density of nano precipitates. Two populations of precipitates could be identified, very fine 10-30nm in size, likely γ' precipitates, and larger elongated precipitates, likely γ" , ~150nm in length.

The microstructure of the as-printed ruptured specimen tested at 650°C, 650MPa for 385h was quite different with the presence of the typical cell structure observed in LPBF 718 (Figure 5). The Nb rich precipitates are consistent with Taller et al. [11] observation of δ precipitate and laves phase in the as-printed LPBF 718. Similar to what was observed in the annealed specimen, cracking took place at grain boundaries with the presence of creep cavitation voids. Very fine nano precipitates were observed, 10 to 30nm in size, very similar to the as fabricated specimens observed in the as-printed condition by Taller et al. [11]. Further analysis is needed to quantify the γ' to the γ" precipitates in the as-printed and annealed creep tested specimens.

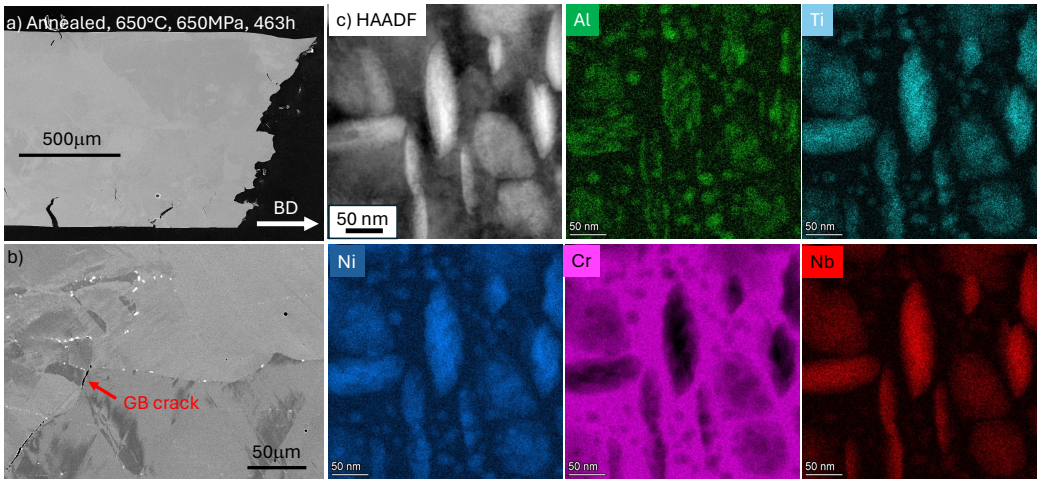

Figure 4: Annealed LPBF 718 specimen creep tested at 650°C, 650MPa, a) and b) BSE-SEM micrographs in the rupture area highlighting cracking at grain boundary, c) high-angle annular dark-field (HAADF) STEM and associated composition maps

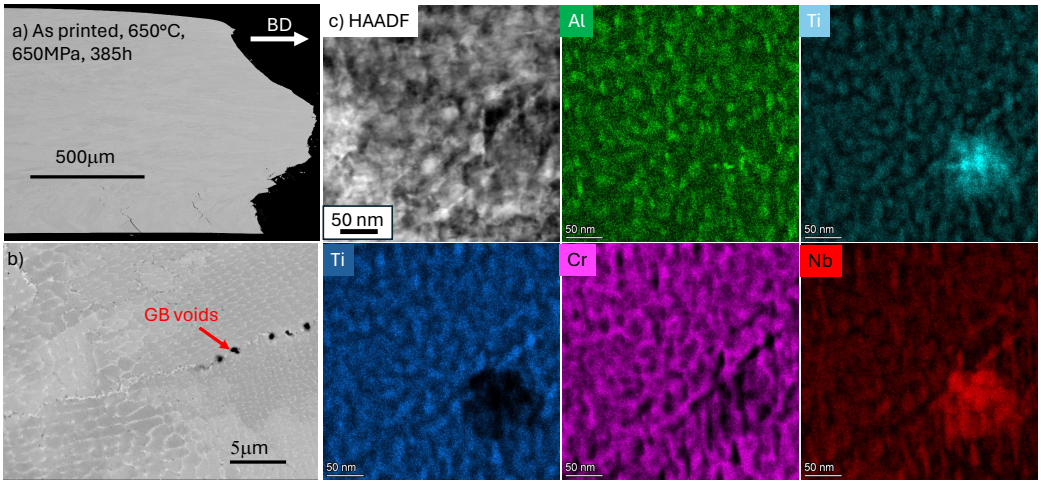

Figure 5*:* As-printed LPBF 718 specimen creep tested at 650°C, 650MPa, a) and b) BSE-SEM micrographs in the rupture area highlighting the presence of a cell structure and voids at grain boundaries, c) HAADF STEM micrograph and associated composition maps

Creep testing of LPBF282

As can be seen in Figure 6, optical micrographs of the LPBF282 specimens revealed a low volume fraction of flaws for the T1, T3 and T5 specimens, but a high-volume fraction for the C1, C3 and C5 specimens. Analysis of the in-situ images generated during printing (Figure 6e) indicated that particle spattering might explain such a variation in flaw density with spatter particles being detected more frequently in the Cs specimens compared to the Ts specimens. 3D visualization of the XCT scans of the C3 and T3 specimens before and after testing are shown in Figure 7a. The higher volume fraction of flaws for the C3 specimen compared to the T3 specimen was confirmed over the entire gage section with flaw volume fractions of 0.14% and 0.01%, respectively. Flaw

numbers with respect to their size are given in Figure 7b. Only 42 flaws between 50µm -250µm in size were detected in T3 versus 881 for C3. Creep curves are shown in Figure 7d for LPBF 282 specimens tested at 750°C with an applied stress of 300MPa or 350MPa. Similar creep rates were measured for the Cs and Ts specimens, but the tertiary stage started earlier and ductility at rupture was lower for the high-flaw C specimens, leading to slightly lower lifetime. The C5 and T5 specimens were interrupted after 546h to perform XCT scans before failure. Overall, the LPBF282 specimens exhibited slightly lower lifetime and significantly lower ductility compared with wrought 282 [33].

As can be seen in Figure 7a, XCT scans after creep testing for the C3 and T3 specimens revealed a significant increase in the number of flaws less than 250µm in size compared to the XCT scans before testing. This increase was more significant for the C3 specimen, from 881 to 2377 flaws counted for C3 compared to an increase from 42 to 230 for the T3 specimen. These creep cavitation flaws might be linked to flaws too small to be detected before testing, with their size increasing during creep testing. The number of these small flaws is likely higher in the Cs specimens compared to the Ts specimens. Another plausible explanation for the formation of a higher number of flaws in C3 compared to T3 is that other microstructural differences exist between the two specimens leading to more creep cavitation nucleation sites for the C3 specimen. Microstructure characterization is ongoing to assess this hypothesis.

While the number of large flaws did not increase significantly, Figure 7c highlights a significant increase in flaw size for flaws >250µm in equivalent diameter. A few of the initial large flaws were located close to the rupture area for both the C3 and T3 specimens and ongoing work is aiming at the registration of each initial flaw to track its shape change after creep testing and assess the impact of each flaw on specimen failure. The main goal is to correlate the flaw distribution with the alloy creep behavior to improve creep lifetime modeling.

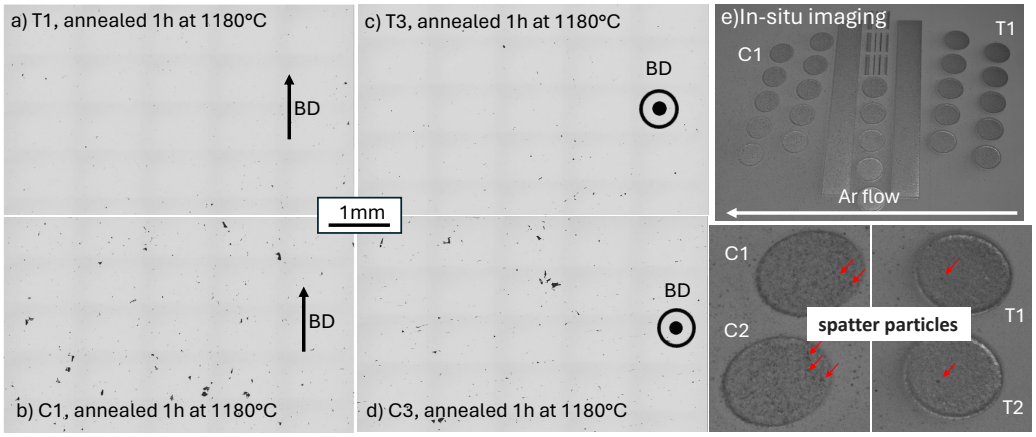

Figure 6: a) to d) Optical micrographs of the LPBF282 alloy after annealing for 1h at 1180°C, a) T1 specimen, along the BD, b) C1 specimen, along the BD, c) T3 specimen, perpendicular to the BD, C3, specimen, perpendicular to the BD, e) in situ images acquired during printing

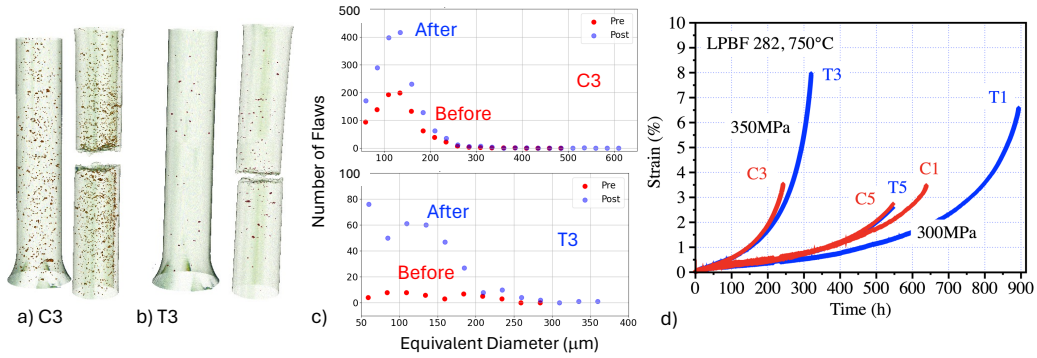

Figure 7: 3D visualization of the flaws detected by XCT before and after creep testing, a)C3 specimen b) T3 specimen, c) number of flaws in the C3 and T3 specimens before and after creep testing, d) Creep curves for the LPBF282 tested at 750°C with an applied stress of 300 or 350MPa. C5 and T5 were interrupted after 546h.

CONCLUSIONS

To selected Ni-based alloys relevant to the AMMT program and the NE community, work was performed on low Co 718 alloy, high strength high temperature 617, 230, 625 and 282 alloys, and low Cr molten salt compatible Hastelloy N and 244 alloys. The high creep strength of the LPBF 718 alloy in the annealed and as printed conditions was attributed to the formation of γ' and γ'' precipitates. These precipitates can form during printing, after heat treatment or during creep testing at 600-650°C. Formation of brittle s at grain boundaries resulted in low ductility for all the creep tested specimens. Printing of crack free 617 and 230 by LPBF could not be achieved due to hot tearing and composition change would like be needed. While alloy 230 exhibited great room temperature tensile properties, along the build direction with very high yield strength, ductility was significantly reduced perpendicular to the build direction due to the presence of cracks. As expected, the fabrication of crack-free LPBF 625 using similar printing parameters was achieved, highlighting the excellent printability of the alloy. The growing interest in alloy 625 from the NE community and the acceptable high temperature strength and corrosion resistance in addition to the alloy printability make LPBF 625 an exciting Ni-based alloy for the AMMT program that will be further characterized. The γ' strengthened alloy 282 was fabricated by LPBF and creep tested at 750°C. Flaws did not impact the alloy secondary creep rates but likely played a role in low ductility and slightly reduced lifetimes of the LPBF 282 specimens. XCT scans were used to corelate specimen flaws with creep properties, and ongoing analysis will pro

Two Ni-based alloys of interest for the nuclear industry, alloys 718 and 282, were fabricated by laser powder bed fusion for creep evaluation at 600°C and 650°C. LPBF 718 exhibited creep strength similar to the creep strength of wrought 718 in the annealed condition, and slightly lower creep strength in the as-printed condition, with no effect of the specimen orientation with respect to the build direction. Low ductility at rupture was, however, observed for all the LPBF 718 specimens. The alloy creep strength was attributed to the formation of nano γ' and γ'' precipitates both in the as-printed and annealed specimens, and formation of brittle precipitates at grain boundaries led to preferential grain boundary cracking and low ductility. For annealed LPBF 282, variation in the initial flaw volume fraction from one specimen to another did not impact creep

rates at 750°C but resulted in lower creep ductility and slightly lower creep lifetime for the higher flaw specimens. In situ data generated during printing highlighted particles spattering that might explain variation of flaws within the same build. XCT scans before and after creep testing revealed different creep cavitation behavior between the specimen with high and low initial flaw volume fraction.

ACKNOWLEDGMENTS

The authors would like to thank T. Lowe, J. Moser, B. Abbot and D. Newberry for their help with experimental efforts, as well as Sam Bell and Amanda Heimbrook for technical review of this manuscript. This work was sponsored by the U.S. Department of Energy's Office of Nuclear Energy, Advanced Materials and Manufacturing Program.

REFERENCES

[1] M. Li, D. Andersson, R. Dehoff, A. Jokisaari, I. Van Rooyen, and D. Cairns-Gallimore, "Advanced Materials and Manufacturing Technologies (AMMT), 2022 Roadmap", ANL report, ANL-23/12 (2022).

[2] I. Gibson, D. Rosen, B. Stucker, M. Khorasani, "Additive Manufacturing Technologies", Vol. 17 Springer (2021).

[3] M. Griffiths, Chapter 9, "Ni-based alloys for reactor internals and steam generator applications", Structural Alloys for Nuclear Energy Applications, Edited by G. R. Odette and S. J. Zinkle (2019).

[4] 18. T. Yonezawa, "Nickel-Based Alloys," in Comprehensive Nuclear Materials, 7, 319-354 (2020).

[5] J. Serp, M. Allibert, O. Benes, S. Delpech, O. Feynberg, V. Ghetta, D. Heuer, D. Holcomb, V. Ignatiev, J. L. Kloosterman, L. Luzzi, E. Merle-Lucotte, J. Uhlír, R. Yoshioka, D. Zhimin, "The molten salt reactor (MSR) in generation IV: Overview and perspectives," Progress in Nuclear Energy 77 (2014) 308-319.

[6] S. Dryepondt, S. Taller, F. List, Z. Snow, M. McMurtrey, M. Moorehead, M. Mulholland, Srinivas Aditya Mantri, Prioritization of Existing Reactor Materials, 2023, ORNL/TM-2023/3108.

[7] A. Kracke, "Superalloys, the most successful alloy system of modern times – Past, Present and future", Proceedings of the 7th International Symposium on Superalloy 718 and its derivatives, Edited by E.O Ott et al., TMS (The Minerals, Metals & Material Society), 13-50 (2010).

[8] K. Gruber a, W. Stopyra, K. Kobiela, B. Madejski, M. Malicki, T. Kurzynowski, "Mechanical properties of Inconel 718 additively manufactured by laser powder bed fusion after industrial high-temperature heat treatment", Journal of Manufacturing Processes, 73, 642-659 (2022).

[9] E. M. Fayed, M. Saadati, D. Shahriari, V. Brailovski, M. Jahazi, & M. Medraj, “Effect of homogenization and solution treatments time on the elevated-temperature mechanical behavior of Inconel 718 fabricated by laser powder bed fusion”, Scientific Reports, 11, 2020 (2021).

[10] X. Li, J.J. Shi, C.H. Wang, G.H. Cao, A.M. Russell, Z.J. Zhou, C.P. Li, G.F. Chen, “Effect of heat treatment on microstructure evolution of Inconel 718 alloy fabricated by selective laser melting”, Journal of Alloys and Compounds, 764, 639-649 (2018).

[11] S. Taller and T. Austin, “Using post-processing heat treatments to elucidate precipitate strengthening of additively manufactured superalloy 718”, Additive Manufacturing”, 60, 103280 (2022).

[12] L. Huang, Y. Cao, J. Zhang, X. Gao, G. Li, Y. Wang, “Effect of heat treatment on the microstructure evolution and mechanical behaviour of a selective laser melted Inconel 718 alloy”, Journal of Alloys and Compounds 865, 158613 (2021).

[13] Y. Gao, D. Zhang, M. Cao, R. Chen, Z. Feng, R. Poprawe, J.H. Schleifenbaum, S. Ziegler, “Effect of δ phase on high temperature mechanical performances of Inconel 718 fabricated with SLM process”, Mater. Sci. Eng. A. 767, 138327 (2019).

[14] E. Hosseini and V.A. Popovich, “A review of mechanical properties of additively manufactured Inconel 718”, Additive Manufacturing, 30, 100877 (2019).

[15] M. Komarasamy, S. Shukla, S. Williams, K. Kandasamy, S. Kelly, R.S. Mishra, “Microstructure, fatigue, and impact toughness properties of additively manufactured nickel alloy 718”, Additive Manufacturing 28, 661-675, (2019).

[16] Kevinsanny, S. Okazaki, O. Takakuwa, Y. Ogawa, Y. Funakoshi, H. Kawashima, S. Matsuoka, H. Matsunaga, “Defect tolerance and hydrogen susceptibility of the fatigue limit of an additively manufactured Ni-based superalloy 718”, International Journal of Fatigue 139, 105740 (2020).

[17] S. Sanchez, C. Hyde, I. Ashcroft, G. Ravi, A. Clare, “Multi-laser scan strategies for enhancing creep performance in LPBF”, Additive Manufacturing 41, 101948 (2021).

[18] Y.-L. Kuo, S. Horikawa, K. Kakehi, “Effects of build direction and heat treatment on creep properties of Ni-base superalloy built up by additive manufacturing”, Scripta Materialia 129, 74-78 (2017).

[19] Y.-L. Kuo, T. Nagahari, K. Kakehi, “The effect of post-processes on the microstructure and creep properties of Alloy718 built up by selective laser melting”, Materials 11, 6, 996 (2018).

[20] S. Wu, H.Z. Peng, X. Gao, P.D. Hodgson, H.Y. Song, Y.M. Zhu, Y. Tian, A.J. Huang, “Improving creep property of additively manufactured Inconel 718 through specifically-designed post heat treatments”, Materials Science & Engineering A 857, 144047 (2022).

[21] L.M. Pike, “Development of a fabricable gamma-prime strengthened superalloy”, in: R.C. Reed, K.A. Green, P. Caron, T.P. Gabb, M.G. Fahrmann, E.S. Huron, Shiela A. Woodard (Eds.), In Superalloys 2008, 191–200 (2008).

[22] K.A. Christofidou, H.T. Pang, W. Li, Y. Pardhi, C.N. Jones, N.G. Jones, H.J. Stone, “Microstructural control and optimization of Haynes 282 manufactured through laser powder bed fusion”, in: S. Tin, M. Hardy, J. Clews, J. Cormier, Q. Feng, J. Marcin, C. O’Brien, A. Suzuki (Eds.), Superalloys 2020, Springer International Publishing, Cham, 1014-1023 (2020).

[23] R. Rajan, Raytheon Technologies Research Center “Developing an Ultra-Compact, Topology-Optimized Heat Exchanger using Additive Manufacturing”, ARPA-E project.

[24] C. Magnin, Z. Islam, M. Elbakhshwan, A. Brittan, D. J. Thoma. M. H.Anderson, “The performance of additively manufactured Haynes 282 in supercritical CO2”, Materials Science & Engineering A 841, 143007 (2022).

[25] Z. Islam, A. Kumar, A.B. Rankouhi, C. Magnin, M.H. Anderson, F.E. Pfefferkorn and D.J. Thoma, “A High-Throughput Method to Define Additive Manufacturing Process Parameters: Application to Haynes 282”, Metallurgical and Materials Transactions A, 53, 250-263 (2022).

[26] J. Boswell, J. Jones, N. Barnard, D. Clark, M. Whittaker, R. Lancaster, “The effects of energy density and heat treatment on the microstructure and mechanical properties of laser additive manufactured Haynes 282”, Materials & Design 205, 109725(2021).

[27] K.A. Unocic, D. Shin, X. Sang, E. Cakmak, P.F. Tortorelli, “Single-step aging treatment for a precipitation-strengthened Ni-based alloy and its influence on high-temperature mechanical behavior”, Scripta Materialia 162, 416-420 (2019).

[28] A. Ziabari, S.V. Venkatakrishnan, Z. Snow, A. Lisovich, M. Sprayberry, P. Brackman, C. Frederick et al. "Enabling rapid X-ray CT characterisation for additive manufacturing using CAD models and deep learning-based reconstruction."npj Computational Materials 9, no. 1 (2023): 91.

[29] Haynes 718 Alloy, in Haynes International Corporation (2020).

[30] Inconel alloy 718, Special Metals, Publication Number SMC-045

[31] M. Chang, A.K. Koul, P. Au, and T Terada, “Damage Tolerance of Wrought Alloy 718 Ni.Fe-Base Superalloy”, Journal of Materials engineering and Performance, 3, 356-366 (1994).

[32] C. R. Brinkman’, M. K. Booke, and J. L. Ding, “Creep and Creep-rupture behavior of alloy 718”, Proceedings of Superalloys 718,625 and Various Derivatives, Edited by Edward A. Iaria, The Minerals, Metals & Materials Society, 519-536 (1991).

[33] B. A. Pint, Hong Wang, C. Shane Hawkins, Kinga A. Unocic, “Technical Qualification of New Materials for High Efficiency Coal-Fired Boilers and Other Advanced FE Concepts: Haynes® 282® ASME Boiler and Pressure Vessel Code Case”, ORNL report, ORNL/TM-2020/1548 (2020).